



Acoustically driven degradation in single crystalline silicon solar cell

O.Ya. Olikh

Faculty of Physics, Taras Shevchenko National University of Kyiv, Kyiv 01601, Ukraine

ARTICLE INFO

Article history:

Received 18 January 2018

Received in revised form 10 March 2018

Accepted 12 March 2018

Available online xxx

Keywords:

Silicon

Solar cells

Ultrasound influence

ABSTRACT

The influence of ultrasound on current–voltage characteristics of crystalline silicon solar cell was investigated experimentally. The transverse and longitudinal acoustic waves were used over a temperature range of 290–340 K. It was found that the ultrasound loading leads to the reversible decrease in the photogenerated current, open–circuit voltage, fill factor, carrier lifetime, and shunt resistance as well as the increase in the ideality factor. The experimental results were described by using the models of coupled defect level recombination, Shockley–Read–Hall recombination, and dislocation–induced impedance. The contribution of the boron–oxygen related defects, iron–boron pairs, and oxide precipitates to both the carrier recombination and acousto–defect interaction was discussed. The experimentally observed phenomena are associated with the increase in the distance between coupled defects as well as the extension of the carrier capture coefficient of complex point defects and dislocations.

© 2018.

1. Introduction

The silicon solar cells (SSCs) are still dominant in the photovoltaic field due to their high efficiency, low selling price and process maturity. The material properties driving is a top priority for most of manufacturers of SSC or another semiconductor devices. For example, the loss in the SSC efficiency is observed due to illumination (the light–induced degradation or LID in the c–Si case [1–4] and the carrier-induced degradation or CID in the mc–Si case [5,6]), high voltage (the potential–induced degradation or PID [7–9]), or irradiation (the radiation–induced degradation or RID [10,11]). The degradation reason is a changing of crystal defects. That is a transformation of the boron–oxygen or copper–contained complex (in LID case), a decoration of the stacking faults by the positive ions, predominantly sodium, (in PID case) or a creation of the radiation recombination centers (in RID case). The annealing at an elevated temperature is quite often required for efficiency recovery.

At the same time, the ultrasound (US) can effectively interact with defects in silicon. It was experimentally observed that US can cause transformation of impurity and radiation defects [12–17], modification of spectrum [18] and density [19] of surface states, changing of carrier diffusion length [20,21], variation of current in barrier structures [22–27]. Hence, it is expected that ultrasound–induced degradation (USID) can be originated by the acoustic wave (AW) action. After AW propagation had stopped, the full recovery of material properties was often observed without annealing [12,20–22]. Therefore, the USID is expected to be a reversible at room temperature in contrast to rest of degradations.

The aim of our work is to investigate experimentally the acoustically induced (AI) variation of crystalline SSC photo–electrical parameters. Ultrasound was found to result in a decrease in the solar cell efficiency. The US intensity did not exceed 0.5 W/cm² and the USID full recovery was observed at room temperature. The USID dependencies on the AW both type and intensity are presented. The experimentally observed phenomena are associated with the decrease in the carriers lifetime and in the shunt resistance as well as the increase in the ideality factor. To describe the processes in the space charge region (SCR) and in the

Email address: olikh@univ.kiev.ua (O.Ya. Olikh)

diode base as well as to study shunt resistance, we used the models of coupled defect level recombination [28,29], Shockley–Read–Hall (SRH) recombination and dislocation–induced impedance [30,31], respectively. The observed AI phenomena are accounted for in terms of the defect interaction with the AW strain field [32,33].

2. Experimental and calculation details

2.1. Samples

The SSC was fabricated from 2 in. (300 μm thick) p-type boron doped Czochralski silicon wafer with $\langle 111 \rangle$ orientation and a doping level of $1.4 \times 10^{15} \text{ cm}^{-3}$. The n^+ emitter with a carrier concentration of about 10^{19} cm^{-3} and a thickness of 0.5 μm was formed by phosphorus implantation. The wafer surface was capped by the TiO_x antireflective coating. The front grid and rear full area aluminium electrodes were deposited by screen printing before rapid annealing.

The samples used in the experiment were cut from the wafer and mainly differed in the shunt resistance (R_{sh}) value. The typical results for the samples with low ($R_{sh} \approx 10^4 \Omega \cdot \text{cm}^2$ at room temperature) and high ($R_{sh} > 10^{15} \Omega \cdot \text{cm}^2$) values are only presented in the article. These samples are labeled “SC4” and “SC15”, respectively, from now on.

2.2. Ultrasound loading

In case of ultrasound loading (UL), the transverse or longitudinal AWs, which were excited by using LiNbO_3 piezoelectric transducer, were applied to the samples in the $[111]$ -direction. The transducer was attached to a full-area Al back contact. The acoustic contact was made by using the glue “BF-6”. The US frequencies f_{US} , intensities W_{US} , amplitudes of lattice deformation $\xi_{US} = \sqrt{2W_{US}/\rho_{Si} \theta_{US}^3}$, and lattice atom displacements $u_{US} = \sqrt{W_{US}/2 \pi^2 f_{US}^2 \rho_{Si} \theta_{US}}$ are listed in Table 1. $\rho_{Si} = 2.33 \text{ g/cm}^3$ is the silicon density, θ_{US} is the US velocity, 9850 m/s and 5840 m/s in cases of longitudinal and transverse AWs, respectively.

It was reported previously [13,21,27] that the characteristic time of change in silicon structure parameters under the US action did not exceed $2 \times 10^{-3} \text{ s}$. In order to wait until the AI transitional period is completed, the following experimental procedure was used. When UL started, the sample was first exposed to room temperature for 60 min and then the measurement and the sample heating were started. In order to avoid the effect of piezoelectric field on both the measurements and sample parameters, the transducer was shielded. The more details about the experimental setup are presented elsewhere [27].

2.3. Current–voltage measurements and SSC parameters determination

The dark and illuminated forward current–voltage (J – V) characteristics of the samples both with and without UL were measured over a temperature range of 290–340 K. The temperature was controlled by differential copper–constantan thermocouple. Some of the obtained curves are shown in Fig. 1.

The short-circuit current density J_{sc} , open-circuit voltage V_{oc} and the fill factor FF were estimated from the illuminated J – V curve by the conventional mode.

The double-diode model of n^+ –p SSC J – V characteristics is expressed in the following form:

$$J(V, T) = -J_{ph} + \frac{qn_i d}{2\tau_g} \left\{ \exp \left[\frac{q(V - JR_s)}{n_{id} kT} \right] - 1 \right\} + \frac{qn_i^2}{p_p} \sqrt{\frac{\mu_n kT}{\tau_n}} \left\{ \exp \left[\frac{q(V - JR_s)}{kT} \right] - 1 \right\} + \frac{V - JR_s}{R_{sh}}, \quad (1)$$

where J_{ph} is the photogenerated current density, n_i is the intrinsic carrier concentration, τ_g is the SCR carrier lifetime, d is the SCR thickness:

Table 1
The ultrasound loading parameters.

f_{US} (MHz)	wave type	W_{US} (W/cm ²)	ξ_{US} (10^{-6})	u_{US} (nm)	UL label	subjected samples
8.0	longitudinal	0.18	1.3	0.3	IUL	SC4, SC15
4.2	transverse	0.19	2.8	0.6	tULa	SC15
4.2	transverse	0.22	3.1	0.7	tULb	SC4
4.2	transverse	0.40	4.2	0.9	tULc	SC4, SC15

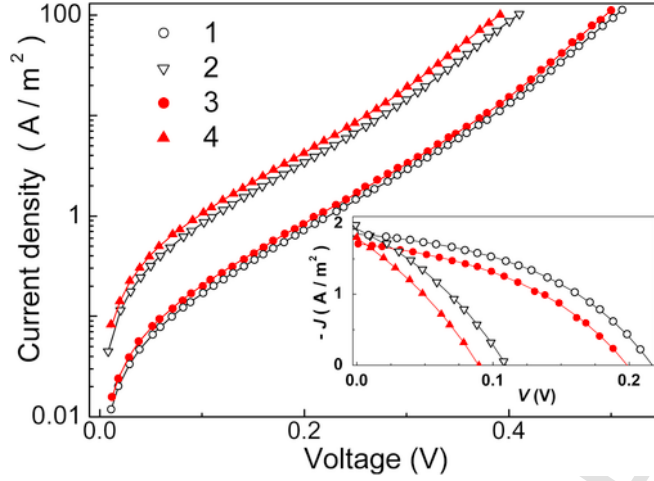


Fig. 1. Dark J - V characteristics measured at 301 K (curves 1, 3, circles) and 341 K (curves 2, 4, triangles) with (2, 4, filled marks, tULc) and without (1, 3, open marks) UL. Inset: Parts of illuminated J - V characteristics over a voltage range of 0– V_{oc} . The marks are the experimental results, and the lines are the curves fitted by Eqs. (1) and (2).

$$d(V, T) = \sqrt{\frac{2\epsilon\epsilon_0(p_p + n_n)}{qp_p n_n} \left[\frac{E_g}{q} - \frac{kT}{q} \ln \left(\frac{N_v N_c}{p_p n_n} \right) - \frac{2kT}{q} - V \right]}, \quad (2)$$

ϵ is the permittivity (11.7 for Si), p_p and n_n are the majority carrier concentration in the p - and n -type regions, E_g is the semiconductor band gap, N_c and N_v are the effective density of states in the conduction and valence bands; n_{id} is the ideality factor, R_s is the series resistances, and μ_n and τ_n are the mobility and lifetime of the electron (minority carrier) in the diode base. The current-voltage equation that models the solar cell by an equivalent electrical circuit contains several parameters related to physical phenomena occurring in the device. It is commonly believed that $J_{0base} = (qn_i^2/n_n) \sqrt{\mu_n kT/\tau_n}$ is closely related to the recombination in the quasi-neutral region, while $J_{0SCR} = (qdn_i/2\tau_g)$ describes the overall SCR recombination.

We used Eqs. (1) and (2) to fit the experimental data taking τ_g , τ_n , n_{id} , R_{sh} , R_s , and J_{ph} (for illuminated J - V curves only) as the fitting parameters. Also, we used the known [34–36] temperature dependences of n_i , E_g , and μ_n . As a result, we obtained extremely good fit to the experimental data — see Fig. 1. The parameters values, obtained from the dark and illuminated measurement at the same temperature and UL option, were identical practically. This concordance is quite expected at low illumination intensity [37].

It is known that $J_{sc} \approx J_{ph} R_{sh} / (R_{sh} + R_s)$. Typical values for SSC R_s are between 0.5 and 2 $\Omega \cdot \text{cm}^2$ [38,39]. The value of R_s was found to be about 1.5 $\Omega \cdot \text{cm}^2$, whereas R_{sh} exceeded 4 $\text{k}\Omega \cdot \text{cm}^2$. Therefore it is expected that $J_{sc} \approx J_{ph}$. In fact, this relation was observed for the J_{ph} , which was obtained by fitting of whole of J - V curve, and the J_{sc} , which was obtained as a point of intersection of a J - V curve with a current axis.

To evaluate the US influence the relative change of parameters were used: $\epsilon_P = (P_{in} - P_{US})/P_{in}$, where P is one of the set $\{J_{sc}, V_{oc}, FF, \tau_g, \tau_n, R_{sh}\}$, subscripts “US” and “in” indicate the values obtained at the same temperature with and without UL, respectively. The AI change of the ideality factor was characterized by the absolute value $\Delta n_{id} = n_{id,in} - n_{id,US}$.

2.4. Illumination

The monochromatic ($\lambda = 900$ nm) and low-intensity light was used for the SSCs illumination. It is known [40] that illumination with intensity of above 0.01 suns can lead to defect formation in p -type silicon. Our work was devoted to investigation of AI effects and the light intensity of $W_{ph} = (8 \pm 4) \text{ W/m}^2$ was chosen to avoid any current induced degradation processes. The light monochromatism allowed to simplify the short-current dependence. In case of used wavelength, the photocurrent defined by the electron-hole pairs generation in the p -region mainly. If the base is several minority carrier diffusion lengths $L_n = \sqrt{\mu_n kT \tau_n / q}$, the J_{sc} can be written as [36,41].

$$J_{sc} = \frac{W_{ph}(1-M)q\beta\lambda}{hc} \frac{\alpha L_n}{1 + \alpha L_n}, \quad (3)$$

where α is the absorption coefficient, M is the reflection coefficient, β is the quantum yield coefficient. We used Eq. (3) to fit the experimental $J_{sc}(T)$ data taking L_n as the fitting parameter. Also, we used the known [36] temperature dependence of α and supposed that β and M were temperature independent, $L_n \propto T^{0.5}$. The last relation was obtained from J - V curves fitting — see Sec. 3.3. Thus, L_n and τ_n can be obtained from the both single J - V curve and J_{sc} temperature dependence. To separate the second case values, the subscript “ph” was used: L_n^{ph} , τ_n^{ph} , $\epsilon_{\tau n}^{ph}$ etc.

2.5. Defect structure modification

To determine the major recombination centers in the investigated samples, the following experimental procedure was used after the AI effects investigation. The samples were light soaked under intensive illumination by a halogen lamp (2 Suns) at approximately 305 K. The illumination time varied from 1 h to 8 h. After illumination was terminated, the sample was exposed to room temperature in the darkness. Over 5 h period, dark J - V characteristics were measured with the interval of 10–15 min in order to determine the kinetics of the parameters at room temperature. To estimate the permanent light-induced change, the measurements of dark J - V characteristics were performed in 48 h after illumination. After the total time under intensive illumination ran up to 15 h, the samples were annealed at 200 °C for 10 min in darkness, after which the measurements were carried out at room temperature. Then, the illumination and measurements were repeated.

2.6. Fitting procedure

All non-linear fittings were done by using the differential evolution method [42–44]. The least-squares method was used to linear fitting.

3. Results and discussion

3.1. Photo-electric conversion

The obtained temperature dependences of the short-circuit current density, open-circuit voltage and the fill factor are shown in Fig. 2. The parameters values at 320 K are listed in Table 2. It should be noted that not only I_{sc} and V_{oc} but also SSC efficiency, FF , and minority carrier lifetime decreases under low-intensity light conditions [38,45–47]. Hence, data in Fig. 2 and Table 2 are not equivalent to the standard test condition (AM1.5, 25 °C, 1000 W/m²) results, but illustrate the AI effects. Note

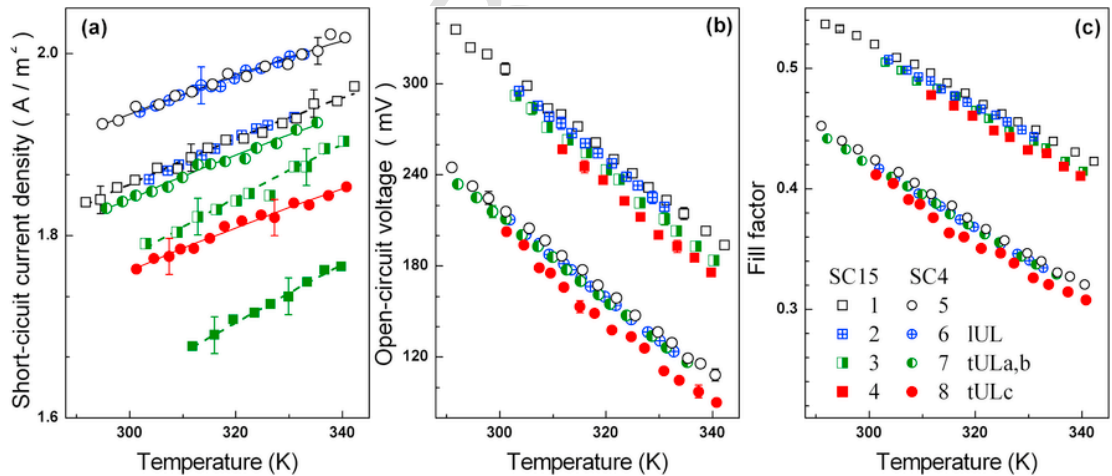


Fig. 2. Temperature dependences of short-circuit (a), open-circuit voltage (b) and fill factor (c) for SC15 (squares) and SC4 (circles). The curves 1 and 5 (open marks) are obtained without UL, curves 2 and 6 correspond to IUL, curve 3 corresponds to tULa, curve 7 corresponds to tULb, curves 4 and 8 correspond to tULc. The marks are the experimental results, and the lines are the curves fitted by Eq. (3).

Table 2

The determined SSC parameters (at 320 K).

Parameter	SC15				SC4			
	Ultrasound loading				Ultrasound loading			
	non	IUL	tULa	tULc	non	IUL	tULb	tULc
J_{sc} (0.01 A/m ²)	191°± °2	191°± °2	184°± °2	171°± °2	198°± °2	198°± °2	189°± °2	181°± °2
V_{oc} (mV)	256°± °4	250°± °4	243°± °4	233°± °4	164°± °4	159°± °4	157°± °4	141°± °4
FF (10 ⁻³)	475°± °2	468°± °2	463°± °2	458°± °2	372°± °2	366°± °2	366°± °2	353°± °2
L_n^{ph} (μm) ^a	99°± °5	92°± °5	67°± °4	55°± °3	125°± °6	124°± °6	103°± °5	98°± °5
L_n (μm)	93°± °5	82°± °4	47°± °3	34°± °2	106°± °5	99°± °5	80°± °4	69°± °4
τ_n^{ph} (10 ⁻⁷ s) ^a	31°± °3	26°± °3	14°± °2	9°± °1	49°± °5	48°± °5	33°± °4	30°± °3
τ_n (10 ⁻⁷ s)	26°± °3	21°± °3	7°± °2	3.5°± 0.7	35°± °3	31°± °3	20°± °3	15°± °2
τ_g (10 ⁻⁹ s)	70°± °4	66°± °3	57°± °3	48°± °2	35°± °2	31°± °2	30°± °2	29°± °2
E_{tg} (meV) ^a	242°± °7	237°± °5	234°± °5	234°± °5	246°± °6	234°± °5	241°± °5	243°± °5
n_{id} (± 0.01)	2.59	2.60	2.61	2.63	2.51	2.52	2.54	2.54
T_{id} (K) ^a	226°± °8	215°± °10	243°± °15	233°± °15	327°± °10	319°± °15	308°± °20	358°± °25
K_{US} (m ⁻² s ⁻¹)	(3.3°± 0.5)×10 ²⁴				(5.0°± 0.2)×10 ²³			
R_{sh} (kΩ·cm ²)	> 10 ¹²	> 10 ¹²	> 10 ¹²	> 10 ¹²	12°± °1	13°± °1	10°± °1	8°± °1

^aDetermined by using the whole temperature range.

that the yearly averaged energy yield of a solar panel, especially if operated in the middle Europe, strongly depends on its low light-level performance.

Fig. 2 shows an acoustically driven degradation of the short-circuit current, open-circuit voltage, and fill factor. The parameters relative changes are listed in Table 3. We would like to stress that, firstly, all found AI effects are reversible. In other word, the J_{sc} , V_{oc} , FF , and another parameters, which are described above, revert to the initial value after the UL termination and sample storage for about 24 h at room temperature. The reversibility testifies that ultrasound neither causes defect diffusion nor changes defect concentration. Secondly, the AI relative changes are weakly depend on temperature over the explored range.

The US intensities of IUL, tULa, and tULb are close. But it is shown by J_{sc} and V_{oc} data that the tULa,b result in the more prominent AI parameter changes. At the same time, IUL and tULa,b differ in the both f_{US} and u_{US} (ζ_{US}). It was previously shown [23,48] that US influence on the silicon structures should arose with the f_{US} increase. Therefore the efficiency of US action on the SSC is determined by the atom displacement (lattice deformation) mainly and the transverse AWs are more effective influence tool.

Table 3

The acoustically induced change of SSC parameters.

Parameter	SC15			SC4		
	IUL	tULa	tULc	IUL	tULb	tULc
$\varepsilon_{J_{sc}}$ (%)	0°± °1	4°± °1	10°± °1	0°± °1	5°± °1	9°± °1
$\varepsilon_{V_{oc}}$ (%)	2°± °2	5°± °2	9°± °2	3°± °2	4°± °2	14°± °2
ε_{FF} (%)	2°± °1	3°± °1	4°± °1	2°± °1	2°± °1	5°± °1
$\varepsilon_{L_n^{ph}}$ (%)	7°± °7	32°± °7	44°± °7	1°± °7	18°± °7	22°± °7
ε_{L_n} (%)	12°± °6	49°± °6	63°± °6	6°± °6	25°± °6	35°± °6
$\varepsilon_{\tau_n^{ph}}$ (%)	16°± °15	55°± °15	70°± °15	2°± °15	33°± °15	39°± °15
ε_{τ_n} (%)	19°± °12	73°± °12	87°± °12	11°± °12	43°± °12	57°± °12
ε_{tg} (%)	6°± °5	19°± °5	31°± °5	9°± °5	14°± °5	17°± °5
Δn_{id} (10 ⁻²)	1°± °1	2°± °1	4°± °1	1°± °1	3°± °1	3°± °1
$\varepsilon_{R_{sh}}$ (%)				-8°± °10	17°± °10	33°± °10

Eq. (3) show that J_{sc} strongly depends on a carrier diffusion length. The determined by fitting L_n^{ph} , calculated τ_n^{ph} values, and its changes are given in Tables 2 and 3. The fitting results are shown on Fig. 2(a) by curves. Thus the US effects the minority carrier lifetime.

Unfortunately the analytical expressions for V_{oc} and FF are absent in the double-diode model case. But Eq. (1) show that the open-circuit voltage and fill factor depend on τ_n , n , τ_g , and R_{sh} . The next three Sections are devoted to the consideration of US influence on these parameters. The reasons of V_{oc} and FF change are discussed in Section 3.5.

3.2. Space charge region

The parameters of I - V characteristics associated with SCR phenomena are n_{id} and τ_g . The temperature dependences of the SCR carrier lifetime and ideality factor are shown in 3(a) and 3(b), respectively. The thermoactivated growth of SCR lifetime is observed over the explored temperature range — see 3(a). The measured temperature dependence of τ_g is well described by the following equation

$$\tau_g(T) = \tau_{g0} \exp\left(-\frac{E_{\tau g}}{kT}\right). \quad (4)$$

As shown in Fig. 3(b), the ideality factor decreases with the increase in temperature, and the dependence of n_{id} on $1/T$ is close to linear. Thus, dependence $n_{id}(T)$ can be expressed as

$$n_{id}(T) = n_{id,\infty} + T_{id}/T. \quad (5)$$

The values of T_{id} and $E_{\tau g}$ found for samples under UL as well as without UL are listed in Table 2.

As seen from Fig. 3 and Table 2,

- (i) UL leads to the increase in n_{id} and decrease in τ_g ; the AI changes are listed in Table 3;
- (ii) τ_g and n_{id} are varied by tUL more effectively; $E_{\tau g}$ and Δn_{id} increase with W_{US} enhancement;
- (iii) UL does not affect $E_{\tau g}$ and T_{id} values; $E_{\tau g}$ is equal to 0.24 ± 0.01 eV; T_{id} depends on sample and is equal to 330 ± 30 K (in the SC4 case) or 230 ± 20 K (in the SC15 case).

For the purpose of our analysis, it is important to discuss the recombination mechanism in SCR of the investigated samples. At first, the large n_{id} value and small τ_g value should be accentuated. According to classical SRH theory, the ideality factor must be smaller than 2, and τ_g temperature dependence is expected [49,50] to be described by the relation

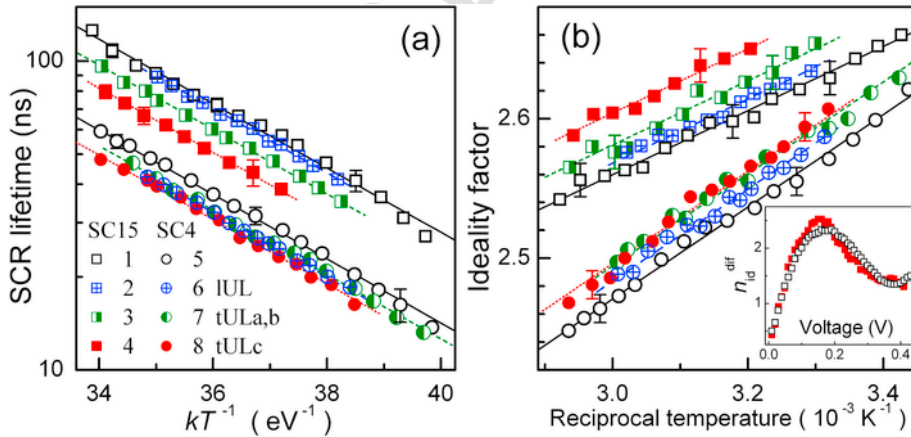


Fig. 3. Temperature dependences of SCR carrier lifetime (a) and ideality factor (b) for SC15 (curves 1–4, squares) and SC4 (5–8, circles). The curves 1 and 5 (open marks) are obtained without UL, and curves 2 and 6 correspond to IUL, curve 3 corresponds to tULa, curve 7 corresponds to tULb, curves 4 and 8 correspond to tULc. The marks are the experimental results, and the lines are the fitted curves using Eq. (4) and $E_{\tau g} = 0.24$ eV (a) or Eq. (5) and $T_{id} = 330$ or 230 K (b). Inset: Two examples of voltage dependences of differential ideality factor for SC15. The open marks are obtained without UL, full mark correspond to tULc. $T = 335$ K.

$$\tau_g \simeq 2 \tau_n \sqrt{\sigma_n / \sigma_p} \cosh [(E_t - E_i) / kT] \quad (6)$$

where σ_n , σ_p , and E_t are the electron and hole capture cross sections (CCSs) and the energy level of the recombination center, and E_i is the intrinsic energy level. In our case, n_{id} is greater than 2, and τ_g increases with temperature. Therefore, SRH theory cannot be applied in our case.

Several attempts to account for large n_{id} value have been made by using different models. According to van der Heide et al. [51], the nonuniform contact resistance of the front side metallisation leads to a high n_{id} value. However, this theory predicts the dependence of ideality factor on light intensity, whereas n_{id} change with W_{ph} is not observed in our case. Beier and Voss [52] explain the large n_{id} by the saturation effects within the SRH-model. However, this theory is unable to explain the J_{0SCR} magnitude, which is much greater than expected for a silicon. The large ideality factor is attributed to the deep-level-assisted tunneling [53,54] too. But according to this model, the n_{id} does not depend on temperature.

At the same time, all the observed features of SCR recombination can be explained by the model of coupled defect level recombination (CDLR) [28,29,38,55,56]. According to the CDLR model, the recombination is the result of carrier exchange between two defect levels and crystal bands; and the high ideality factor is due to saturation of the inter-level recombination channel, leading to a hump in the $n_{id}^{dif} = \frac{1}{kT} \frac{dV}{d(\ln I)} = f(V)$ characteristics. Such hump is observed in the our case — see inset in Fig. 3(b). It was found that the magnitude and the position of this hump strongly depends on the energy positions and on the capture and inter-level recombination parameters of the two levels involved [29,38]. In particular, it is supposed [29] that the recombination rate is dominant at the sites where acceptor-like defect is coupled with donor-like defect. In a simplified case, when there is no carrier exchange between the donor level E_t^D and valence band, as well as between the acceptor level E_t^A and conduction band, the recombination rate R can be expressed [28] as

$$R = \frac{R_{12} - \sqrt{R_{12}^2 - 4\tau_n^D \tau_p^A (np - n_i^2)(1 - \varepsilon)}}{2\tau_n^D \tau_p^A (1 - \varepsilon)}, \quad (7)$$

$$R_{12} = \frac{(n + n_D)(p + p_A)}{R_{DA}} + \tau_n^D (p + p_D) + \tau_p^A (n + n_A), \quad (8)$$

$$\tau_n^D = (N_D \sigma_n^D v_{th,n})^{-1}, \quad \tau_p^A = (N_A \sigma_p^A v_{th,p})^{-1}, \quad (9)$$

where R_{DA} is the coupling parameter, N_D and N_A are the densities of donor and acceptor-like defects, σ_n^D and σ_p^A are the electron CCS of the donor and hole CCS of the acceptor, $v_{th,n}$ and $v_{th,p}$ are the thermal electron and hole velocities, $n_{D,A}$, $p_{D,A}$, and ε depend on E_t^D , E_t^A , and level degeneracy factors.

According to Steingrube et al. [29], CCS for defect in a pair differs from that for an isolated defect and depends on the distance r between the donor and the acceptor:

$$\sigma_{n,p}^{D,A}(r) \propto r^2, \quad (10)$$

R_{DA} is proportional to the overlap integral of the defect wave functions as well. If both defects are characterized by the H-like radial-symmetric wave function and equal Bohr radius a_0 , the following expression can be used [29].

$$R_{DA}(r) \propto N_D N_A \left[1 + \frac{r}{a_0} + \frac{1}{3} \left(\frac{r}{a_0} \right)^2 \right] e^{-r/a_0}. \quad (11)$$

Unfortunately, the equation does not account for the functional relation between J - V characteristics parameters and attributes of defects taking part in CDLR. However, it is shown [28,55] that n_{id} increases with the decrement in R_{DA} . Since $\tau_g \propto R^{-1}$, the $n_{D,A}$, $p_{D,A}$, and ε are expected to provide a thermoactivated behavior of SCR lifetime. In our opinion, the value of E_{tg} is mainly determined by couple component energy levels, whereas the value of T_{id} is affected by N_D and N_A too. Hence, (i) same defects are take part in the SCR recombination in both SC15 and SC4 because the E_{tg} values are identical; (ii) the defect concentrations in

SC15 and SC4 are different because the T_{id} , $\tau_{g,in}$, and $n_{id,in}$ values are different; (iii) UL does not result in the modification of the level position as well as defect concentration because the $E_{\tau g}$ and T_{id} values are not affected.

In our opinion, the observed reversible AI modifications of n_{id} and τ_g are induced by donor–acceptor distance alteration in the samples under UL. In fact, according to the data [32,33], the force acting on a point defect during UL can be expressed as

$$F_d = \chi \Delta\Omega_d \frac{\partial \xi(x, t)}{\partial x}, \quad (12)$$

where χ is the bulk elasticity modulus, $\Delta\Omega_d$ is the crystal volume change per defect (e.g. $\Delta\Omega_d < 0$ and $\Delta\Omega_d > 0$ for the vacancy and interstitial atom, respectively), ξ is the crystal lattice deformation, and AW propagates along x axis, $\partial \xi(x, t)/\partial x \propto \xi_{US}$. Therefore, a point defect vibrates under UL, so oscillation amplitude and phase are determined by both the defect character and AW intensity.

The simplest model, which is shown in Fig. 4, gives the following qualitative conclusion. Initially, the donor (D) and the acceptor (A) are separated by the distance r_{in} . Under UL, the defects would vibrate with amplitudes u_D and u_A . Depending on ξ_{US} , defect elastic strain ($\Delta\Omega_d^D$ and $\Delta\Omega_d^A$), and defect coupling the defect vibration amplitudes can have different values. The vibration axis coincides with AW displacement direction and forms angle φ with the line, which passes through the defect initial positions. δ is the phase shift between donor and acceptor vibration.

We use Eqs. (10) and (11) to estimate AI relative changes of CCS $\varepsilon_\sigma = [\sigma_{US} - \sigma(r_{in})]/\sigma(r_{in})$ and coupling parameters $\varepsilon_{RDA} = [R_{DA,US} - R_{DA}(r_{in})]/R_{DA}(r_{in})$, where σ_{US} and $R_{DA,US}$ are averaged over the AW period. The results of simulation are shown in Figs. 5 and 6. In this estimation, the relaxation time in the CDLR sub-system is assumed to be considerably shorter than f_{US}^{-1} , and we apply the previously used [29] value $a_0 = 3.23$ nm. In addition, the chosen u_D and u_A values are commensurate

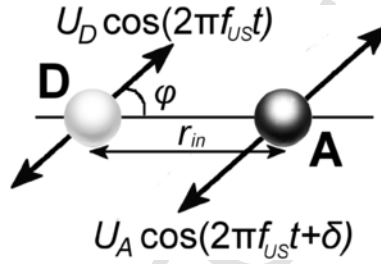


Fig. 4. Model of CDLR center behavior under US action.

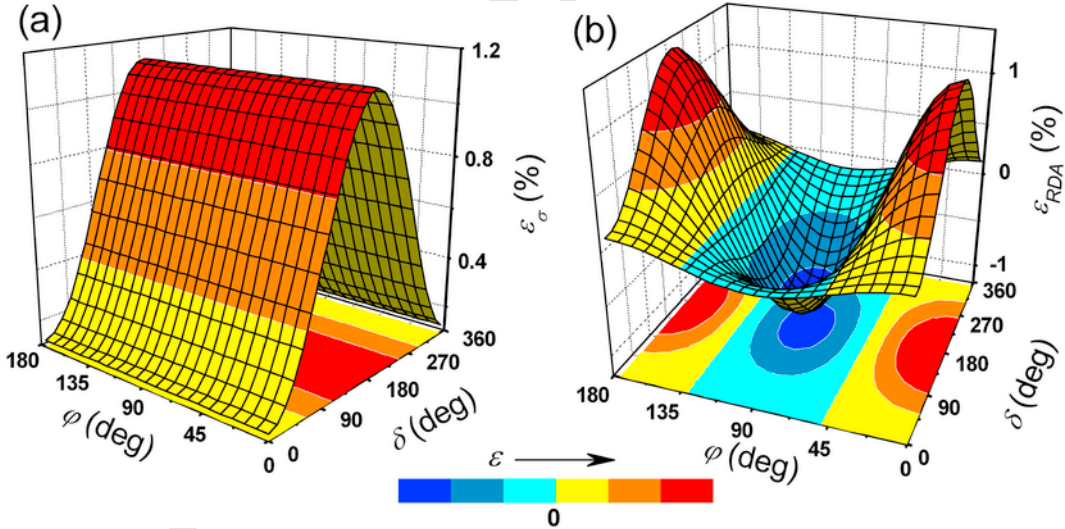


Fig. 5. Simulated dependencies of AI changes of capture cross section (a) and coupling parameter (b) on the vibration phase shift and AW displacement direction. The parameters are set to $a_0 = 3.23$ nm, $r_{in} = 10$ nm, $u_A = 1$ nm, and $u_D = 0.5$ nm.

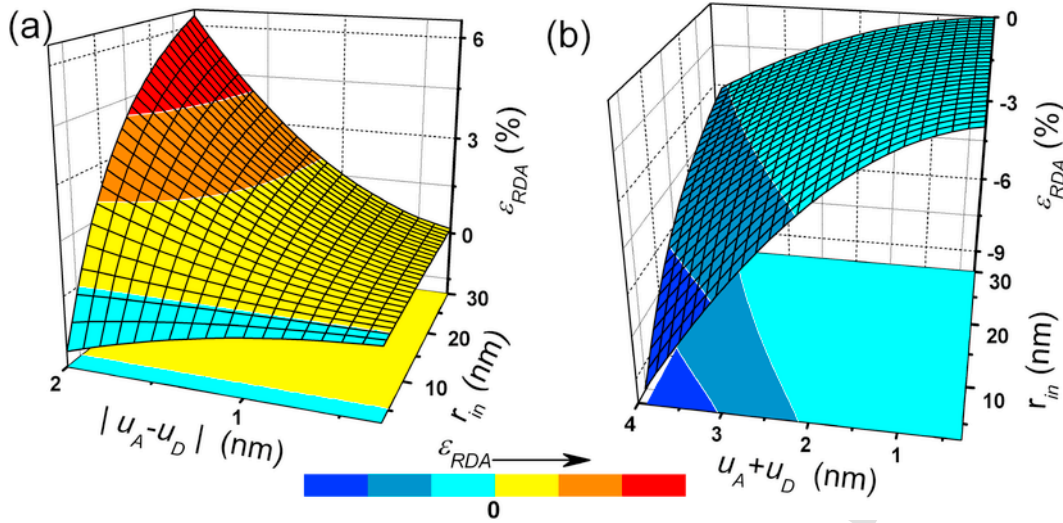


Fig. 6. Simulated dependencies of AI changes of coupling parameter on the vibration amplitudes and initial donor–acceptor distance. The parameters are set to $\varphi = 0^\circ$, $\delta = 0^\circ$ (a), and $\varphi = 90^\circ$, $\delta = 180^\circ$ (b).

with u_{US} . However, it should be taken into account that the displacement of the point defect without the covalent bond could exceed a matrix atom displacement.

Fig. 5(a) show that the UL leads to the increase in SSC. The AI alteration of coupling parameter is more complicated — see Fig. 5(b). In particular, the decrease in R_{DA} is expected in case of $\varphi \approx 90^\circ$ [the couple axis is perpendicular to the AW displacement direction, see Fig. 6(b)] or in case of low r_{in}/a_0 value [see Fig. 6(a)]. In the lat case, the intensive CDLR is expected [28,29].

Thus, according to the our model estimation, UL causes the donor–acceptor distance change and results in ε_σ and ε_{RDA} , which mainly depend on lattice deformation. According to the CDLR theory, the increase in the SSC and decrease in the coupling parameters should lead to the decrease in the carrier lifetime and increase in the ideality factor. It was observed in the experiment.

3.3. Quasi-neutral region

Base lifetime describes the processes which occur in the quasi-neutral region of the solar cell. Fig. 7 shows τ_n behavior in the explored temperature range. As expected, minority carrier lifetime increases as the temperature increases. The determined by fitting τ_n , calculated L_n values, and its changes are given in Tables 2 and 3. The obtained values of $L_{n,in}$ are comparable with the

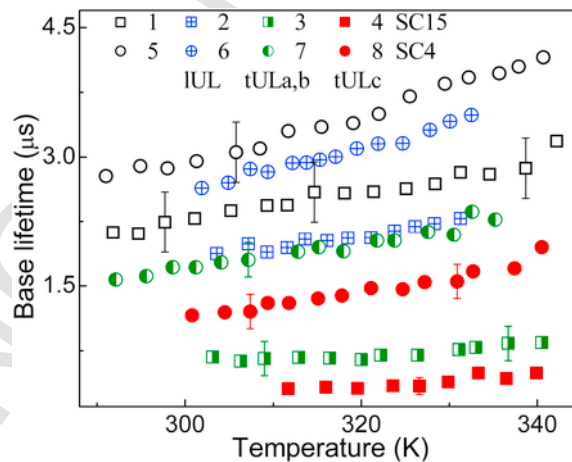


Fig. 7. Temperature dependences of base lifetime for SC15 (curves 1–4, squares) and SC4 (5–8, circles). The curves 1 and 5 (open marks) are obtained without UL, and curves 2 and 6 correspond to IUL, curve 3 corresponds to tULa, curve 7 corresponds to tULb, curves 4 and 8 correspond to tULc.

$L_{n,in}^{ph}$ values. The small quantitative difference between the ϵ_{Ln}^{ph} and ϵ_{Ln} values, in our opinion, deals with the AI change of the L_n temperature dependence, which is not taken into account during the $J_{sc}(T)$ fitting.

The calculation shows that the both band-to-band recombination and Auger recombination can be neglected in the investigated samples. Therefore, the SRH recombination should be only under consideration. In case of the low injection level, SRH lifetime is described by the following equation

$$\tau_n^{-1} = \sum_i \tau_{n,i}^{-1} = \sum_i N_{d,i} \sigma_{n,i} v_{th,n}, \quad (13)$$

where $\tau_{n,i}$ characterizes lifetime due to recombination by i -th defect, and $N_{d,i}$ and $\sigma_{n,i}$ are the concentration and electron CCS of i -th defect, respectively.

Fig. 7 shows that UL results in a decrease in τ_n . As AI changes are reversible, the lifetime alteration, in our opinion, deals with the increase in σ_n under US action. The majority of recombination center in the silicon are known to be a complex point defect and a complex components are not the same. Following the empirical relation proposed in Ref. [57], we assume that Eq. (10) is valid for a complex point defect as well. In this case, however, r is the distance which separates the components of a complex. According to the model suggested in Sec. 3.2, UL leads to r variation. In the case of CDLR, AI change of the capture cross section of donor (or/and acceptor) is supplemental to the variation of both the coupling parameter and the couple distance, but only CCS change determines the AI variation of base lifetime. If no US absorption by the defect is assumed, δ is equal to 0° if $(\Delta\Omega_d^D \cdot \Delta\Omega_d^A) > 0$ or to 180° if $(\Delta\Omega_d^D \cdot \Delta\Omega_d^A) < 0$. In this simple case, relative changes of CCS depend on oscillation amplitudes and do not depend on φ :

$$\epsilon_\sigma = (u_D \pm u_A)^2 / 2 r_{in}^2, \quad (14)$$

where “+” and “−” correspond to $\delta = 180^\circ$ and $\delta = 0^\circ$, respectively.

The defects in silicon structures are not all acoustically active (AA) and can remain unmodified under the action of ultrasound. The acousto-defect interaction efficiency depends on the defect type and structure [15,16]. If only one AA center with N_d^{AA} and σ_n^{AA} is present in the sample, Eq. (13) for τ_n^{-1} under UL takes the following shape:

$$\tau_{n,US}^{-1} = \tau_{n,in}^{-1} + \epsilon_\sigma N_d^{AA} \sigma_n^{AA} v_{th,n} = \tau_{n,in}^{-1} + K_{US} u_{US}^2, \quad (15)$$

where K_{US} characterizes the complex-ultrasound interaction and depends on properties defects as well as crystal matrix; in particular, $K_{US} \propto N_d^{AA}$. Equation (15) takes into account that $u_D, u_A \propto \zeta_{US} \propto u_{US}$. Eq. (15) is similar to the well-known Messenger–Spratt equation [36], which describes the irradiation-induced decrease in the lifetime.

The obtained dependences of the reciprocal base lifetime versus the AI atom displacements are shown in Fig. 8. The linearity of these dependences proves the correctness of our assumptions. The obtained K_{US} values are listed in Table 2. The greater K_{US} value in SC15 is evident that the AA defect concentration is greater as well.

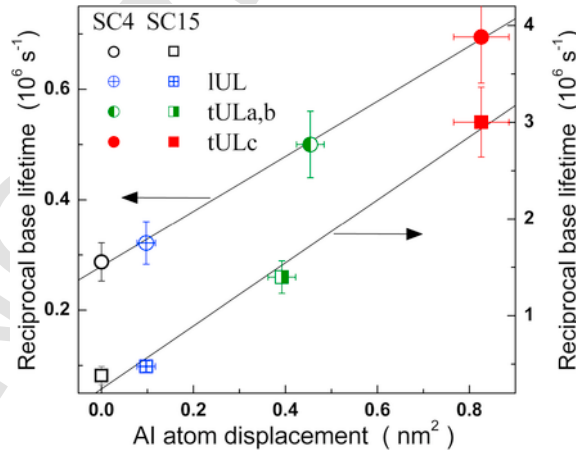


Fig. 8. Dependencies of reciprocal base lifetime on AI lattice atom displacement for SC15 (squares, right axis) and SC4 (circles, left axis) at 320 K. Symbol filling is determined by the AW intensity and type and coincides with Fig. 7 notation. Lines are linear fitting.

It should be noted that an initial distance between the recombination complex components is much less than the donor–acceptor distance in CDLR. Therefore, according to Eq. (14), the more effective US influence is expected in the first case and $\varepsilon_{\tau n} > \varepsilon_{\tau g}$ is observed experimentally.

3.4. Shunt resistance

Fig. 9 shows the shunt resistance over the explored temperature range. As seen from the figure, the tUS results in a decrease in R_{sh} whereas the IUL does not change shunt resistance practically. The calculated data are listed in Tables 2 and 3.

The shunt resistance is known [38,58] to occur in p – n structure due to several non-mechanical reasons. It can be caused by aluminum particles, macroscopic Si_3N_4 inclusions, filaments consisting from cubic SiC, or inversion layers at precipitates. In the course of firing, the Al particle can penetrate into the sample creating p^+ -doped region around it, which compensates the emitter and remains in ohmic contact with the base. Subsequent annealing should decrease R_{sh} , but this expected behavior conflicts with data, which are presented therein after, in Sec. 3.6. SiC filaments, inversion layers, and Si_3N_4 inclusions occur mainly in multicrystalline silicon cells [38,58] and cannot cause shunt resistance in the investigated samples. Dislocations, however, which intersect the junction, are generally held responsible as a possible source of ohmic current [58–60]. Dislocations should be strongly recombinative, its recombination current may become strong enough for it to act as a shunt. For this reason they should be decorated by impurities [58].

According to the model of dislocation-induced impedance of photovoltaic detector suggested by Gopal and Gupta [30,31], R_{sh} can be given by:

$$R_{sh} = \frac{T}{\sigma_{dis}} \left[\cosh \left(\frac{E_{dis} - E_i}{kT} \right) + \cosh \left(\frac{U_s}{kT} \right) \right], \quad (16)$$

with

$$\sigma_{dis} = \rho_{dis} A^2 q^2 A_{dis} \sqrt{K_n K_p} N_{dis} (n_p + p_p) / k, \quad (17)$$

where E_{dis} is the energy level which significantly contributes to the dislocation recombination current, U_s is the potential at the surface of the dislocation core, A is the sample area, ρ_{dis} and A_{dis} are the dislocation density and surface area, respectively, K_n and K_p are the probabilities for electrons and holes capture by the dislocation states, and N_{dis} is the density of surface states at each dislocation. Equation (16) is true for the simplified case of $K_p = K_n$. It should be noted that a similar temperature dependence of a SSC shunt resistance is used elsewhere [61] too.

To fit the experimental data for R_{sh} , we used Eq. (16). As the fitting parameters, $(E_{dis} - E_i)$, U_s , and σ_{dis} were taken. It has been found that the experimental data are in good agreement with the fitting curves (see Fig. 9) for values $(E_{dis} - E_i) = (0.34 \pm 0.02)$ eV and $U_s = (5 \pm 4) \times 10^{-8}$ eV, which were independent of UL. The obtained value of $(E_{dis} - E_i)$ cor-

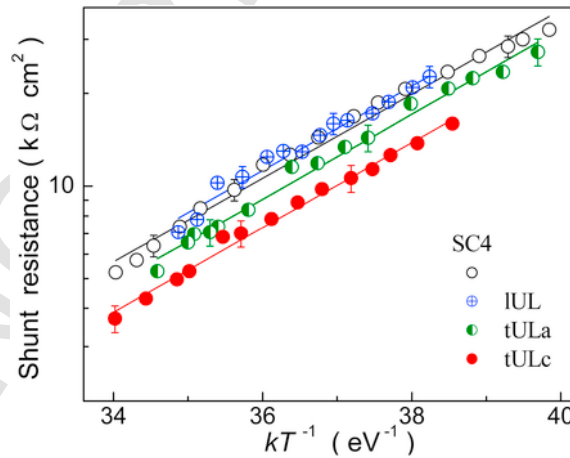


Fig. 9. Temperature dependences of shunt resistance for SC4, obtained with and without (open marks) UL. The marks are the experimental results, and the lines are the fitted curves using Eq. (16).

responds to the carrier activation energy 0.22 ± 0.02 eV and is comparable with the $0.22 \div 0.25$ eV [62], 0.28 eV [63], 0.19 eV [64], and 0.23 eV [65], which was earlier reported for an impurity at the dislocation or with an intrinsic dislocation level.

tUL causes σ_{dis} increase. In our opinion, this is caused by an A_{dis} augmentation. Namely, the dislocation core atom displacement is parallel or normal to the current direction in case of IUL or tUL, respectively. As a result, the carriers are captured by dislocation levels from enlarged volume in the tUL case. Therefore, the effective surface area increases and R_{sh} decreases due to US action.

3.5. Open-circuit voltage and fill factor simulation

In order to visualize dependencies of the open-circuit voltage and fill factor on τ_n , n_{id} , τ_g , and R_{sh} , the following procedure was used. Firstly, we used Eqs. (1)–(3) to simulated J – V characteristics taking the various values of τ_g , τ_n , n_{id} , and R_{sh} . The parameters values, which are close to those of investigated SSCs, are used in simulation. Secondly, V_{oc} and FF were estimated from the obtained J – V curves by the conventional mode. The results are shown in Figs. 10 and 11.

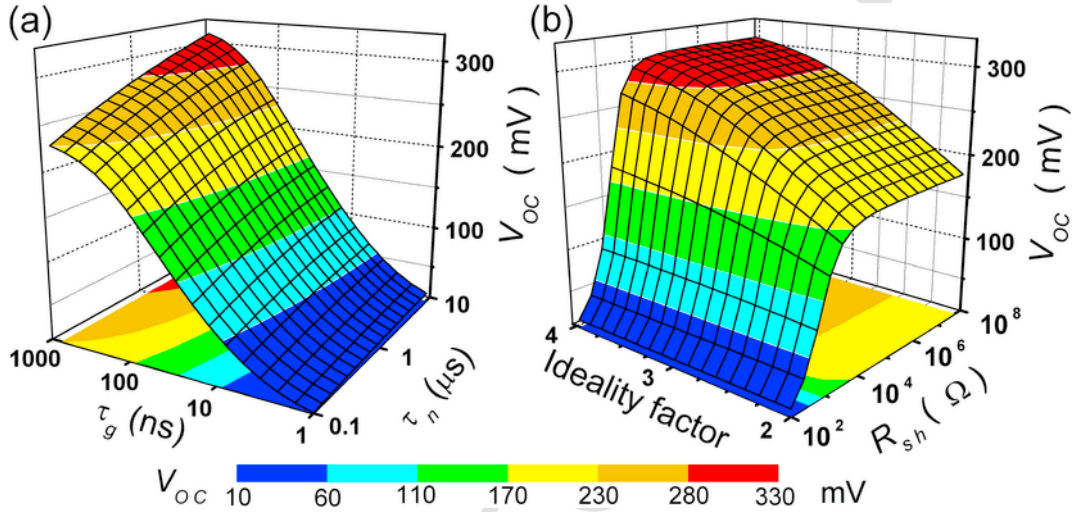


Fig. 10. Simulated open-circuit voltage dependencies on the SCR lifetime and base lifetime (a), and on the ideality factor and shunt resistance (b). The constant values $n = 2.55$ (a), $R_{sh} = 5 \times 10^3 \Omega$ (a), $\tau_n = 3 \times 10^{-6}$ s (b), $\tau_g = 5 \times 10^{-8}$ s (b), and $T = 320$ K were used.

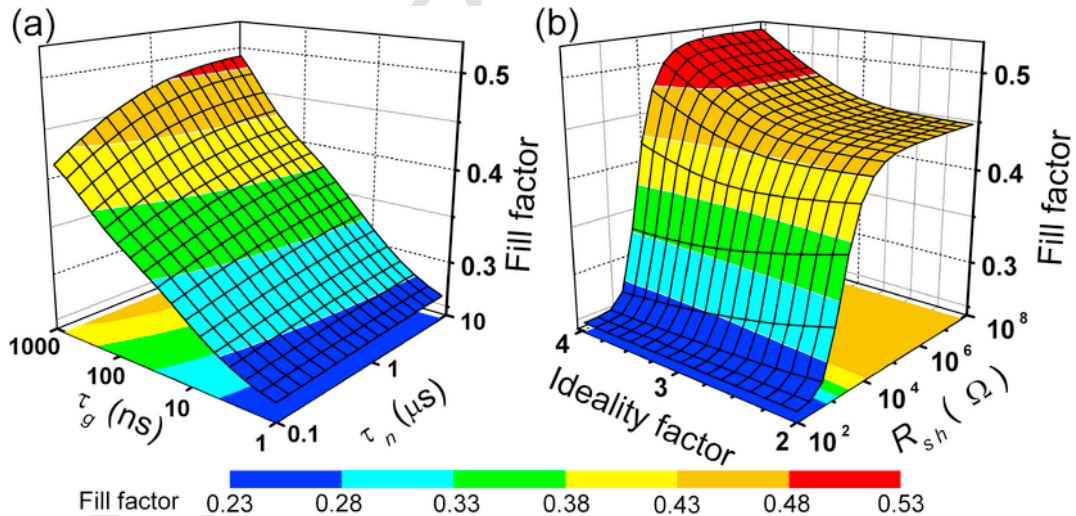


Fig. 11. Simulated fill factor dependencies on the SCR carrier lifetime and base carrier lifetime (a), and on the ideality factor and shunt resistance (b). The constant values $n = 2.55$ (a), $R_{sh} = 5 \times 10^3 \Omega$ (a), $\tau_n = 3 \times 10^{-6}$ s (b), $\tau_g = 5 \times 10^{-8}$ s (b), and $T = 320$ K were used.

As seen from Figs. 10(a) and 11(a), the τ_g decrease leads to the decrease in both V_{oc} and FF . At the same time, the open-circuit voltage and fill factor dependencies on the base lifetime are weak for the investigated SSCs. It should be noted that the W_{ph} value from experiment was used in simulation. If the cell is operated at reduced illumination intensity, then the open-circuit voltage and maximum power point voltage become lower. Hence the recombination current essentially influences V_{oc} and fill factor in contrast to diffusion current [38]. Figs. 10(b) and 11(b) show that V_{oc} and FF are affected by the both n_{id} and R_{sh} , and the effect value considerably depends on shunt resistance value. For instance, V_{oc} increases with the increase in the ideality factor and both V_{oc} and FF does not almost depend on the shunt resistance value if $R_{sh} > 10^5 \Omega$ (in the SC15 case). At the same time, the open-circuit voltage and fill factor decrease with decrease in the shunt resistance, and only FF weakly depends on n_{id} if $R_{sh} \leq 10^4 \Omega$ (in the SCR4 case).

Therefore the discussed above decrease in τ_g leads to AI degradation of the both open-circuit voltage and fill factor. This effect is enhanced by the AI decrease in R_{sh} and partially recovered by the AI increase in n_{id} for SC4 and SC15, respectively.

3.6. Defect type discussions

It is known that main lifetime killers in boron-doped Czochralski-grown Si are boron-oxygen related (BO) defects [2,3], iron-boron pairs [66–68], and oxide precipitates [66,69–73]. The first two defects are sensitive to intensive illumination at room temperature. Intensive light is known [2,3] to cause permanent transformation of BO defects and considerable decrease of minority-carrier lifetime. Annealing at 200 °C for 10 min in the darkness results in both recovery of state and readiness to light-induced degradation of BO defects. At the same time, the vast majority of impurity iron exists in iron-boron pairs. $Fe_i B_s$ can be readily dissociated under intense illumination to release interstitial iron, which results in lifetime changes. In the darkness, $Fe_i B_s$ is repaired and Fe_i concentration decreases according to [66,74].

$$N_{Fe}(t) = (N_{Fe,0} - N_{Fe,eq}) \exp \left[-1.3 \cdot 10^{-3} p_p^{2/3} \exp \left(-\frac{0.68}{kT} \right) t \right] + N_{Fe,eq}, \quad (18)$$

where $N_{Fe,0}$ is the concentration immediately after illumination, and $N_{Fe,eq}$ is the equilibrium concentration which remains for a long time after dissociation.

To inspect a role of BO defects and iron-boron pairs in the investigated samples, the procedure, which is described in Section 2.5, was used. Fig. 12 shows the permanent changes of SSC parameters as a result of the intensive illumination and annealing. In contrast to other, Fig. 12 shows sample SC3 data as well. The SC3 features are the low R_{sh} value and the first 10 min 200 °C annealing before intensive illumination. As seen from the figure, illumination does not result in a considerable permanent change of τ_g , τ_n , and n_{id} before as well as after annealing. Therefore, the BO influence on recombination can be neglected in both the SCR and the base.

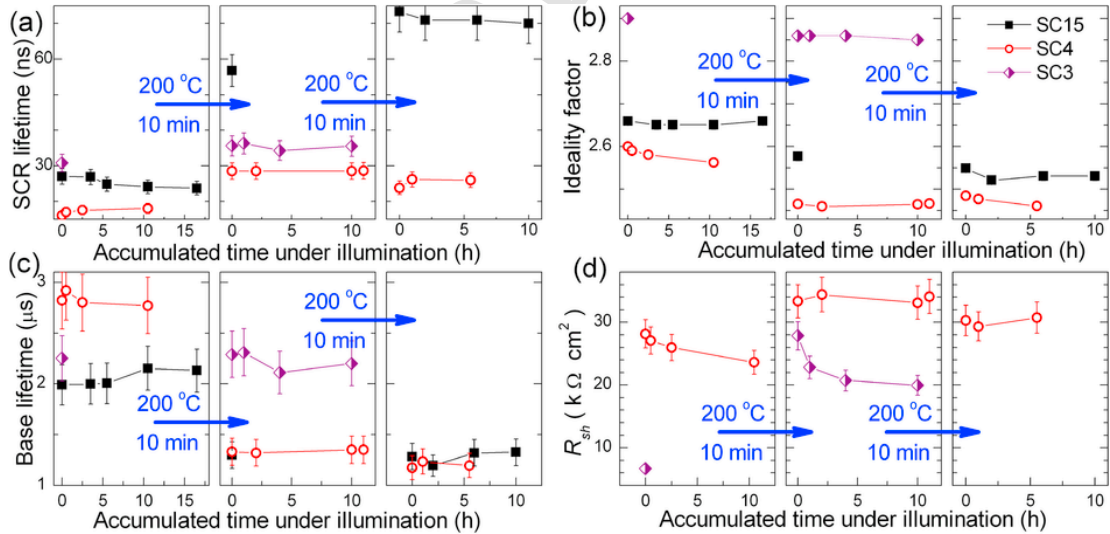


Fig. 12. Dependencies of SCR lifetime (a), ideality factor (b), base lifetime (c), and shunt resistance (d) on accumulated illumination time and annealing. Lines only serve as guide to the eye.

The parameter evolutions after intensive illumination are shown in Fig. 13. Since τ_n does not depend on illumination [see Fig. 13(c)], Fe_iB_s does not influence the base lifetime. It was found that n_{id} increased (by about 0.03) and τ_g decreased (by about 10%) immediately after illumination — see Fig. 13(a, b). These changes vanished gradually. We supposed that τ_g and n_{id} evolutions could be described by expressions similar to Eq. (18). The expected characteristic time 2.53×10^4 s was used, and the fitting lines are presented on Fig. 13(a, b). The fittings with are in good agreement with the experimental data. Hence, it is evident that iron–boron pairs take part in SCR recombination and the acceptor level $E_C - 0.23$ eV is involved in the CDLR. On the one hand, pair Fe_iB_s is a good candidate for an AA center: the B is substitutional impurities whose ionic radius is smaller than that of matrix atoms $\Delta\Omega_d(\text{B}_s) < 0$ whereas the interstitial Fe leads to $\Delta\Omega_d(\text{Fe}_i) > 0$. On the second hand, electron and hole CCS of Fe_i are 1.7 and 0.04 times [66] as much as those of Fe_iB_s . A small τ_g alteration (by about 10%) caused by light is the evidence of the supporting role of iron–boron pair in SCR recombination.

Thus, a conclusion can be made that oxide precipitates are number one agents in SCR and base recombinations. According to Murphy et al. [69,71] there exist at least two independent oxide precipitate related defects. These defects have $\sigma_n/\sigma_p = 157$ and $\sigma_p/\sigma_n = 1200$, respectively [71], which is suitable for CDLR. These facts allow us to conclude that the defect responsible for AI phenomena in iSC is mainly oxide precipitate. Dislocations and stacking faults surround the oxide precipitates and lead to capture coefficient change as well as to increase the concentrations of two defects, without introducing additional states into the bandgap [66,69,71] and assist to defects acousto–activity. The nonuniform distribution of oxide precipitates is observed in the Cz–Si wafer [70] and solar cell [72] and can be a reason of the investigated parameter variation. On the basis of mentioned above, we conclude that the defects, involved in the both recombination and acousto–defect interaction are oxide precipitates mainly.

4. Conclusion

The influence of ultrasound on the silicon solar cell has been investigated experimentally over a temperature range of 290–340 K. The investigation has revealed an acoustically driven reversible degradation in SSC parameters. The effect is intensified in the case of the transverse acoustic waves using. The analysis has shown that degradation is caused by the acoustically induced increase in the carrier capture coefficient for point or extended defects. The qualitative model of the observed phenomenon, which is based on the increase in the distance between coupled defects or between complex defect components due to ultrasound

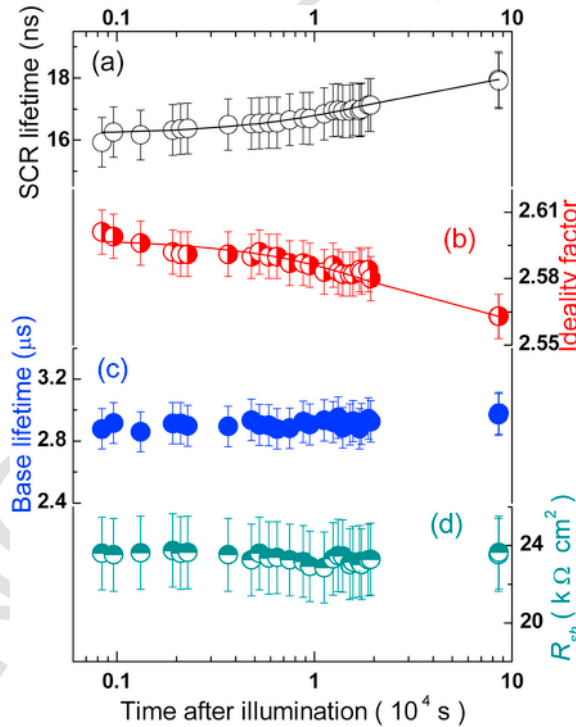


Fig. 13. SCR lifetime (a), ideality factor (b), base lifetime (c), and shunt resistance (d) as a function of time since illumination has stopped. Sample SC4. Lines are plotted by using Eq. (18) and characteristic time 2.53×10^4 s.

action, has been considered. It has been shown that the oxide precipitates are most likely defects, which take part in the acousto-defect interaction. Thus, ultrasound can be an effective tool for controlling silicon structure characteristics.

References

- [1] J. Schmidt, K. Bothe, D. Macdonald, J. Adey, R. Jones, D. Palmer, Electronically stimulated degradation of silicon solar cells, *J. Mater. Res.* 21 (1) (2006) 5–12, <https://doi.org/10.1557/JMR.2006.0012>.
- [2] J. Lindroos, H. Savin, Review of light-induced degradation in crystalline silicon solar cells, *Sol. Energy Mater. Sol. Cells* 147 (2016) 115–126 <https://doi.org/10.1016/j.solmat.2015.11.047>.
- [3] T. Niewelt, J. Schöon, W. Warta, S.W. Glunz, M.C. Schubert, Degradation of crystalline silicon due to boron–oxygen defects, *IEEE J. Photovoltaics* 7 (1) (2017) 383–398, <https://doi.org/10.1109/JPHOTOV.2016.2614119>.
- [4] H. Vahlman, A. Haarahlitonen, W. Kwapil, J. Schon, A. Inglese, H. Savin, Modeling of light-induced degradation due to Cu precipitation in p-type silicon. II. comparison of simulations and experiments, *J. Appl. Phys.* 121 (19) (2017) 195704, <https://doi.org/10.1063/1.4983455>.
- [5] C. Vargas, Y. Zhu, G. Coletti, C. Chan, D. Payne, M. Jensen, Z. Hameiri, Recombination parameters of lifetime-limiting carrier-induced defects in multicrystalline silicon for solar cells, *Appl. Phys. Lett.* 110 (9) (2017) 092106, <https://doi.org/10.1063/1.4977906>.
- [6] D.N.R. Payne, C.E. Chan, B.J. Hallam, B. Hoex, M.D. Abbott, S.R. Wenham, D.M. Bagnall, Acceleration and mitigation of carrier-induced degradation in p-type multi-crystalline silicon, *Phys. Status Solidi RRL* 10 (3) (2016) 237–241, <https://doi.org/10.1002/pssr.201510437>.
- [7] V. Naumann, D. Lausch, A. Hahnel, J. Bauer, O. Breitenstein, A. Graff, M. Werner, S. Swatek, S. Grober, J. Bagdahn, C. Hagendorf, Explanation of potential-induced degradation of the shunting type by Na decoration of stacking faults in Si solar cells, *Sol. Energy Mater. Sol. Cells* 120 (2014) 383–389, <https://doi.org/10.1016/j.solmat.2013.06.015>.
- [8] S. Hoffmann, M. Koehl, Effect of humidity and temperature on the potential-induced degradation, *Prog. Photovoltaics Res. Appl.* 22 (2) (2012) 173–179, <https://doi.org/10.1002/ppp.2238>.
- [9] K. Hara, K. Ogawa, Y. Okabayashi, H. Matsuzaki, A. Masuda, Influence of surface structure of n-type single-crystalline Si solar cells on potential-induced deinflection, *Sol. Energy Mater. Sol. Cells* 166 (2017) 132–139, <https://doi.org/10.1016/j.solmat.2017.03.018>.
- [10] S. Bhat, A. Rao, S. Krishnan, G. Sanjeev, S.E. Puthanveetil, A study on the variation of c-Si solar cell parameters under 8 MeV electron irradiation, *Sol. Energy Mater. Sol. Cells* 120 (2014) 191–196, <https://doi.org/10.1016/j.solmat.2013.08.043>.
- [11] S.Z. Karazhanov, Mechanism for the anomalous degradation of silicon space solar cells, *Appl. Phys. Lett.* 76 (19) (2000) 2689–2691, <https://doi.org/10.1063/1.126445>.
- [12] O. Korotchenkov, H. Grimmliss, Long-wavelength acoustic-mode-enhanced electron emission from Se and Te donors in silicon, *Phys. Rev. B* 52 (20) (1995) 14598–14606, <https://doi.org/10.1103/PhysRevB.52.14598>.
- [13] S.S. Ostapenko, R.E. Bell, Ultrasound stimulated dissociation of Fe–B pairs in silicon, *J. Appl. Phys.* 77 (10) (1995) 5458–5460, <https://doi.org/10.1063/1.359243>.
- [14] O.Y. Olikh, The variation in activity of recombination centers in silicon p–n structures under the conditions of acoustic loading, *Semiconductors* 43 (6) (2009) 745–750, <https://doi.org/10.1134/S1063782609060116>.
- [15] D. Kropman, V. Seeman, S. Dolgov, A. Medvids, Effect of ultrasonic treatment on the defect structure of the Si–SiO₂ system, *Phys. Status Solidi C* 13 (10–12) (2016) 793–797, <https://doi.org/10.1002/pssc.201600052>.
- [16] O.Y. Olikh, A.M. Gorb, R.G. Chupryna, O.V. Pristay-Fenenkov, Acousto-defect interaction in irradiated and non-irradiated silicon n⁺–p structure, *J. Appl. Phys.* 123 (16) (2018) 161573, <https://doi.org/10.1063/1.5001123>.
- [17] Y.M. Olikh, M.D. Tymochko, Reverse ultrasonic changes of electrical conductivity in CdTe:Cl crystals, *Superlattice. Microsc.* 95 (2016) 78–82, <https://doi.org/10.1016/j.spmi.2016.04.038>.
- [18] N. Zaveryukhina, E. Zaveryukhina, S. Vlasov, B. Zaveryukhin, Acoustostimulated changes in the density of surface states and their energy spectrum in p-type silicon single crystals, *Tech. Phys. Lett.* 34 (3) (2008) 241–243, <https://doi.org/10.1134/S106378500803019X>.
- [19] S.A. Mirsagatov, I.B. Sapayeva, Z. Nazarov, Ultrasonic annealing of surface states in the heterojunction of a p–Si/n–CdS/n⁺–CdS injection photodiode, *Inorg. Mater.* 51 (1) (2015) 1–4, <https://doi.org/10.1134/S0020168515010148>.
- [20] S. Ostapenko, Defect passivation using ultrasound treatment: fundamentals and application, *Appl. Phys. Mater. Sci. Process* 69 (2) (1999) 225–232, <https://doi.org/10.1007/s003390050994>.
- [21] I. Ostrovskii, O. Korotchenkov, O. Olikh, A. Podolyan, R. Chupryna, M. Torres-Cisneros, Acoustically driven optical phenomena in bulk and low-dimensional semiconductors, *J. Optic. Pure Appl. Optic.* 3 (4) (2001) S82–S86, <https://doi.org/10.1088/1464-4258/3/4/364>.
- [22] O.Y. Olikh, K.V. Voytenko, R.M. Burbelo, Ultrasound influence on I–V–T characteristics of silicon Schottky barrier structure, *J. Appl. Phys.* 117 (4) (2015) 044505, <https://doi.org/10.1063/1.4906844>.
- [23] O. Olikh, Features of dynamic acoustically induced modification of photovoltaic parameters of silicon solar cells, *Semiconductors* 45 (6) (2011) 798–804, <https://doi.org/10.1134/S1063782611060170>.
- [24] A. Davletova, S.Z. Karazhanov, A study of electrical properties of dislocation engineered Si processed by ultrasound, *J. Phys. Chem. Solid.* 70 (6) (2009) 989–992, <https://doi.org/10.1016/j.jpcs.2009.05.009>.
- [25] A. Davletova, S.Z. Karazhanov, Open-circuit voltage decay transient in dislocation-engineered Si p–n junction, *J. Phys. Appl. Phys.* 41 (16) (2008) 165107, <https://doi.org/10.1088/0022-3727/41/16/165107>.
- [26] V. Melnik, Y. Olikh, V. Popov, B. Romanyuk, Y. Goltvyanskii, A. Evtukh, Characteristics of silicon p–n junction formed by ion implantation with in situ ultrasound treatment, *Mater. Sci. Eng. B: Solid State Mater. Adv. Technol.* 124–125 (2005) 327–330, <https://doi.org/10.1016/j.mseb.2005.08.039>.
- [27] O. Olikh, Reversible influence of ultrasound on γ -irradiated Mo/n-Si Schottky barrier structure, *Ultrasonics* 56 (2015) 545–550, <https://doi.org/10.1016/j.ultras.2014.10.008>.
- [28] A. Schenka, U. Krumbein, Coupled defect-level recombination: theory and application to anomalous diode characteristics, *J. Appl. Phys.* 78 (5) (1995) 3185–3192, <https://doi.org/10.1063/1.360007>.
- [29] S. Steingrube, O. Breitenstein, K. Ramspeck, S. Glunz, A. Schenk, P.P. Altermatt, Explanation of commonly observed shunt currents in c-si solar cells by means of recombination statistics beyond the shockley-read-hall approximation, *J. Appl. Phys.* 110 (1) (2011) 014515, <https://doi.org/10.1063/1.3607310>.
- [30] V. Gopal, S. Gupta, Effect of dislocations on the zero-bias resistance-area product, quantum efficiency, and spectral response of LWIR HgCdTe photovoltaic detectors, *IEEE Trans. Electron. Dev.* 50 (5) (2003) 1220–1226, <https://doi.org/10.1109/TED.2003.813230>.
- [31] V. Gopal, S. Gupta, Contribution of dislocations to the zero-bias resistance-area product of LWIR HgCdTe photodiodes at low temperatures, *IEEE Trans. Electron. Dev.* 51 (7) (2004) 1078–1083, <https://doi.org/10.1109/TED.2004.829857>.
- [32] F. Mirzade, Elastic wave propagation in a solid layer with laser-induced point defects, *J. Appl. Phys.* 110 (6) (2011) 064906, <https://doi.org/10.1063/1.3633524>.

- [33] R. Peleshchak, O. Kuzyk, O. Dan'kiv, Formation of periodic structures under the influence of an acoustic wave in semiconductors with a two-component defect subsystem, *Ukrainian J. Phys.* 61 (8) (2016) 741–746, <https://doi.org/10.15407/ujpe61.08.0741>.
- [34] A.B. Sproul, M.A. Green, Intrinsic carrier concentration and minority-carrier mobility of silicon from 77 to 300 K, *J. Appl. Phys.* 73 (3) (1993) 1214–1225, <https://doi.org/10.1063/1.353288>.
- [35] D.K. Schroder, *Semiconductor Material and Device Characterization*, third ed., John Wiley & Sons, New Jersey, 2006.
- [36] A. McEvoy, T. Markvart, L. Castaner (Eds.), *Solar Cells. Materials, Manufacture and Operation*, second ed., Academic Press, Oxford, 2013.
- [37] O. Breitenstein, S. Riland, A two-diode model regarding the distributed series resistance, *Sol. Energy Mater. Sol. Cells* 110 (2013) 77–86, <https://doi.org/10.1016/j.solmat.2012.11.021>.
- [38] O. Breitenstein, Understanding the current-voltage characteristics of industrial crystalline silicon solar cells by considering inhomogeneous current distributions, *Opto-Electron. Rev.* 21 (3) (2013) 259–282, <https://doi.org/10.2478/s11772-013-0095-5>.
- [39] A. Mette, D. Pysch, G. Emanuel, D. Erath, R. Preu, S.W. Glunz, Series resistance characterization of industrial silicon solar cells with screen-printed contacts using hotmelt paste, *Prog. Photovoltaics Res. Appl.* 15 (6) (2007) 493–505, <https://doi.org/10.1002/pip.755>.
- [40] B.J. Hallam, M.D. Abbott, N. Nampalli, P.G. Hamer, S.R. Wenham, Implications of accelerated recombination–active defect complex formation for mitigating carrier-induced degradation in silicon, *IEEE J. Photovoltaics* 6 (1) (2016) 92–99, <https://doi.org/10.1109/JPHOTOV.2015.2494691>.
- [41] M. Razeghi, A. Rogalski, Semiconductor ultraviolet detectors, *J. Appl. Phys.* 79 (10) (1996) 7433–7473, <https://doi.org/10.1063/1.362677>.
- [42] J. Sun, Q. Zhang, E.P. Tsang, DE/EDA: a new evolutionary algorithm for global optimization, *Inf. Sci.* 169 (3–4) (2005) 249–262, <https://doi.org/10.1016/j.ins.2004.06.009>.
- [43] K. Wang, M. Ye, Parameter determination of Schottky–barrier diode model using differential evolution, *Solid State Electron.* 53 (2) (2009) 234–240, <https://doi.org/10.1016/j.sse.2008.11.010>.
- [44] O.Y. Olikh, Review and test of methods for determination of the Schottky diode parameters, *J. Appl. Phys.* 118 (2) (2015) 024502, <https://doi.org/10.1063/1.4926420>.
- [45] K. Rühle, M.K. Juhl, M.D. Abbott, M. Kasemann, Evaluating crystalline silicon solar cells at low light intensities using intensity-dependent analysis of I–V parameters, *IEEE J. Photovoltaics* 5 (3) (2015) 926–931, <https://doi.org/10.1109/JPHOTOV.2015.2395145>.
- [46] N. Reich, W. van Sark, E. Alsema, R. Lof, R. Schropp, W. Sinke, W. Turkenburg, Crystalline silicon cell performance at low light intensities, *Sol. Energy Mater. Sol. Cells* 93 (9) (2009) 1471–1481, <https://doi.org/10.1016/j.solmat.2009.03.018>.
- [47] F.W. Chen, J.E. Cotter, M.D. Abbott, T.-A. Li, K.C. Fisher, The influence of parasitic effects on injection-level-dependent lifetime data, *IEEE Trans. Electron. Dev.* 54 (11) (2007) 2960–2968, <https://doi.org/10.1109/TED.2007.906970>.
- [48] O. Olikh, K. Voytenko, On the mechanism of ultrasonic loading effect in silicon-based Schottky diodes, *Ultrasonics* 66 (1) (2016) 1–3, <https://doi.org/10.1016/j.ultras.2015.12.001>.
- [49] D. Schroder, The concept of generation and recombination lifetimes in semiconductors, *IEEE Trans. Electron. Dev.* 29 (8) (1982) 1336–1338, <https://doi.org/10.1109/T-ED.1982.20879>.
- [50] H. Aharoni, T. Ohmi, M.M. Oka, A. Nakada, Y. Tamai, Analysis of n+p silicon junctions with varying substrate doping concentrations made under ultra-clean processing technology, *J. Appl. Phys.* 81 (3) (1997) 1270–1288, <https://doi.org/10.1063/1.364442>.
- [51] A.S.H. van der Heide, A. Schonecker, J.H. Bultman, W.C. Sinke, Explanation of high solar cell diode factors by nonuniform contact resistance, *Prog. Photovoltaics Res. Appl.* 13 (1) (2005) 3–16, <https://doi.org/10.1002/pip.556>.
- [52] J. Beier, B. Voss, Humps in dark I–V curves — analysis and explanation, In: *Proceedings of the 23rd IEEE Photovoltaic Specialists Conference*, 1993, pp. 321–326, Louisville, KY, USA.
- [53] J.M. Shah, Y.-L. Li, T. Gessmann, E.F. Schubert, Experimental analysis and theoretical model for anomalously high ideality factors ($n \gg 2.0$) in AlGaIn/GaN p–n junction diodes, *J. Appl. Phys.* 94 (4) (2003) 2627–2630, <https://doi.org/10.1063/1.1593218>.
- [54] A. Kaminski, J.J. Marchand, H.E. Omari, A. Laugier, Q.N. Le, D. Sarti, Conduction processes in silicon solar cells, In: *Proceedings of the 25th IEEE Photovoltaic Specialists Conference*, 1996, pp. 573–576, Washington, DC, USA.
- [55] O. Breitenstein, J. Bauer, P.P. Altermatt, K. Ramspeck, Influence of defects on solar cell characteristics, *Solid State Phenom.* 156–158 (2010) 1–10, <https://doi.org/10.4028/www.scientific.net/SSP.156-158.1>.
- [56] O. Breitenstein, J. Bauer, A. Lotnyk, J.-M. Wagner, Defect induced non-ideal dark i–v characteristics of solar cells, *Superlattice. Microst.* 45 (4–5) (2009) 182–189, <https://doi.org/10.1016/j.spmi.2008.10.025>.
- [57] D.G. Thomas, J. Hopfield, W.M. Augustyniak, Kinetics of radiative recombination at randomly distributed donors and acceptors, *Phys. Rev.* 140 (1A) (1965) A202–A220, <https://doi.org/10.1103/PhysRev.140.A202>.
- [58] O. Breitenstein, J.P. Rakotonianina, M.H. Al Rifai, M. Werner, Shunt types in crystalline silicon solar cells, *Prog. Photovoltaics Res. Appl.* 12 (7) (2004) 529–538, <https://doi.org/10.1002/pip.544>.
- [59] V. Gopal, A new approach to investigate leakage current mechanisms in infrared photodiodes from illuminated current-voltage characteristics, *J. Appl. Phys.* 116 (8) (2014) 084502, <https://doi.org/10.1063/1.4893899>.
- [60] I. Baker, C. Maxey, Summary of HgCdTe 2D array technology in the U.K., *J. Electron. Mater.* 30 (6) (2001) 682–689, <https://doi.org/10.1007/BF02665856>.
- [61] N. Barth, R. Jovanovic, S. Ahzi, M.A. Khaleel, PV panel single and double diode models: optimization of the parameters and temperature dependence, *Sol. Energy Mater. Sol. Cells* 148 (2016) 87–98, <https://doi.org/10.1016/j.solmat.2015.09.003>.
- [62] J. Evans-Freeman, D. Emiroglu, K. Vernon-Parry, J. Murphy, P.R. Wilshaw, High resolution deep level transient spectroscopy applied to extended defects in silicon, *J. Phys. Condens. Matter* 17 (22) (2005) S2219–S2227, <https://doi.org/10.1088/0953-8984/17/22/009>.
- [63] A. Castaldini, D. Cavalcoli, A. Cavallini, S. Pizzini, Experimental evidence of dislocation related shallow states in p-type Si, *Phys. Rev. Lett.* 95 (7) (2005) 076401, <https://doi.org/10.1103/PhysRevLett.95.076401>.
- [64] P. Omeling, E.R. Weber, L. Montelius, H. Alexander, J. Michel, Electrical properties of dislocations and point defects in plastically deformed silicon, *Phys. Rev. B* 32 (10) (1985) 6571–6581, <https://doi.org/10.1103/PhysRevB.32.6571>.
- [65] M. Ogawa, S. Kamiya, H. Izumi, Y. Tokuda, Electronic properties of dislocations introduced mechanically at room temperature on a single crystal silicon surface, *Phys. B Condens. Matter* 407 (15) (2012) 3034–3037, <https://doi.org/10.1016/j.physb.2011.09.139>.
- [66] J.D. Murphy, K. Bothe, M. Olmo, V.V. Voronkov, R.J. Falster, The effect of oxide precipitates on minority carrier lifetime in p-type silicon, *J. Appl. Phys.* 110 (5) (2011) 053713, <https://doi.org/10.1063/1.3632067>.
- [67] V. Vahanissi, A. Haarahiltunen, H. Talvitie, M. Yli-Koski, H. Savin, Impact of phosphorus gettering parameters and initial iron level on silicon solar cell properties, *Prog. Photovoltaics Res. Appl.* 21 (5) (2013) 1127–1135, <https://doi.org/10.1002/pip.2215>.
- [68] J. Schmidt, Effect of dissociation of iron–boron pairs in crystalline silicon on solar cell properties, *Prog. Photovoltaics Res. Appl.* 13 (4) (2005) 325–331, <https://doi.org/10.1002/pip.594>.
- [69] J. Murphy, J. McGuire, K. Bothe, V. Voronkov, R. Falster, Minority carrier lifetime in silicon photovoltaics: the effect of oxygen precipitation, *Sol. Energy Mater. Sol. Cells* 120 (2014) 402–411, <https://doi.org/10.1016/j.solmat.2013.06.018>.
- [70] J. Schön, A. Youssef, S. Park, L.E. Mundt, T. Niewelt, S. Mack, K. Nakajima, K. Morishita, R. Murai, M.A. Jensen, T. Buonassisi, M.C. Schubert, Identification of lifetime limiting defects by temperature- and injection-dependent photoluminescence imaging, *J. Appl. Phys.* 120 (10) (2016) 105703, <https://doi.org/10.1063/1.4961465>.

- [71] J.D. Murphy, K. Bothe, R. Krain, V.V. Voronkov, R.J. Falster, Parameterisation of injection-dependent lifetime measurements in semiconductors in terms of Shockley–Read–Hall statistics: an application to oxide precipitates in silicon, *J. Appl. Phys.* 111 (11) (2012) 113709, <https://doi.org/10.1063/1.4725475>.
- [72] L. Chen, X. Yu, P. Chen, P. Wang, X. Gu, J. Lu, D. Yang, Effect of oxygen precipitation on the performance of Czochralski silicon solar cells, *Sol. Energy Mater. Sol. Cells* 95 (11) (2011) 3148–3151, <https://doi.org/10.1016/j.solmat.2011.06.044>.
- [73] M. Porrini, P. Tessariol, Minority carrier lifetime of p-type silicon containing oxygen precipitates: influence of injection level and precipitate size/density, *Mater. Sci. Eng., B* 73 (1–3) (2000) 244–249, [https://doi.org/10.1016/S0921-5107\(99\)00472-9](https://doi.org/10.1016/S0921-5107(99)00472-9).
- [74] W. Wijaranakula, The reaction kinetics of iron-boron pair formation and dissociation in p-type silicon, *J. Electrochem. Soc.* 140 (1) (1993) 275–281, <https://doi.org/10.1149/1.2056102>.